Insights into the Structure and Dynamics of the Dinuclear Zinc β-Lactamase Site from *Bacteroides fragilis*†

Dimas Suárez

Departamento de Química Física y Analítica, Universidad de Oviedo, Julián Clavería 8, 33006 Oviedo, Spain

Edward N. Brothers and Kenneth M. Merz, Jr.*

152 Davey Laboratory, Department of Chemistry, The Pennsylvania State University, University Park, Pennsylvania 16802-6300

Received December 21, 2001

ABSTRACT: Herein, we report quantum chemical calculations and molecular dynamics (MD) simulations of the dinuclear form of the *Bacteroides fragilis* zinc β-lactamase. We studied four different configurations which differ in the protonation state of the Asp103 residue and in the presence or absence of a Zn1−OH−Zn2 bridge. The flexibility of the Zn1−OH−Zn2 bridge was studied by means of quantum mechanical (QM) calculations on cluster models while the relative stabilities of the different configurations were estimated from QM linear scaling calculations on the enzyme. Contacts between important residues (Cys104, Asp69, Lys185, etc.), the solvation of the zinc ions, and the conformation of the active site β-hairpin loop were characterized by the MD analyses. The influence of the buried sodium ion close to the Zn2 position was investigated by carrying out a secondary simulation where the sodium ion was replaced with an internal water molecule. The comparative structural analyses among the different MD trajectories augmented with energetic calculations have demonstrated that the *B. fragilis* protein efficiently binds the internal Na^+ ion observed crystallographically. Moreover, we found that when Asp103 is unprotonated, a rigid Zn1−OH−Zn2 bridge results, while for neutral Asp103, a fluctuating Zn1−Zn2 distance was possible via the breaking and formation of the Zn1−OH−Zn2 bridge. The mechanistic implications of these observations are discussed in detail.

Bacteria have developed antibiotic resistance strategies in three major ways: production of hydrolytic enzymes known as β-lactamases, changes in the permeability of the cell membrane, and alterations of the target enzymes (*1*, *2*). Among these mechanisms, β-lactamase production, relentlessly fueled by natural selection, is generally considered the primary route of resistance to β-lactam antibiotics. The mechanistic division of β-lactamases is between serine enzymes (*3*, *4*), in which the hydroxyl group of the essential serine acylates the β-lactam substrates, and zinc metalloenzymes, in which zinc ions are crucial for catalysis (*5*−*7*). Although the serine β-lactamases outnumber the zinc enzymes, the zinc β-lactamases have become a major research and clinical problem given that these enzymes efficiently hydrolyze nearly all β-lactams, including the versatile broad-spectrum antibacterial carbapenem derivatives. Moreover, the most widely used inhibitors of serine β-lactamases (e.g., clavulanic acid) are also destroyed by these enzymes (*8*).

The first zinc β-lactamase to be identified was found in the relatively innocuous soil bacterium *Bacillus cereus* in the 1960s. Since then, it has become apparent that zinc β-lactamases are responsible for antibiotic resistance in an increasing number of pathogenic bacteria, including the *Klebsiella*, *Serrattia*, *Chryseobacterium*, *Pseudomonas*/*Stenotrophomonas*, *Aeromonas*, and *Bacteroides* genera (*5*). To date, the occurrence of zinc β-lactamases has not been clinically prevalent, and only a significant percentage of bacteria strains in Asia have been reported to exhibit carbapenem resistance mediated by zinc β-lactamases (*7*, *9*). However, the zinc β-lactamase genes threaten rapid dissemination to other pathogenic bacteria by both plasmid and integron-borne mechanisms. Indeed, the recent appearance of resistance to carbapenems in *Pseudomonas aeruginosa* strains isolated in several European countries may reflect strain or gene dissemination of zinc β-lactamases (*10*−*12*). Unlike the case with the serine β-lactamases, at present there are no known clinically useful inhibitors of the broad-spectrum zinc β-lactamases. These facts clearly stress the urgency and importance of improving our understanding of the zinc β-lactamases to design either new β-lactams with improved activity against bacteria or inhibitors capable of extending the utility and lifetime of already known antibiotics.

The enzyme system studied in this work, the zinc β-lactamase from *Bacteroides fragilis*, binds two zinc ions with equal affinity (*6*). Several independent X-ray structure determinations have been reported for this enzyme (*13*−*16*). In the crystal structure obtained at 1.85 Å (pH 7.0) reported by Concha et al. (*13*), the active site contains a Zn dinuclear

† This work was supported by the NIH through Grant GM44974 and by the National Center for Supercomputer Applications (NCSA) via generous allocations of supercomputer time.

* To whom correspondence should be addressed. E-mail: merz@psu.edu. Fax: (814) 863-8403.

10.1021/bi0121860 CCC: $22.00
Published on Web 04/30/2002

complex in which the distorted tetrahedral (Zn1) and trigonal bipyramidal (Zn2) arrangements are connected (Zn1−Zn2 ∼ 3.5 Å) through a shared water molecule (Wat1), most probably in its deprotonated (hydroxide) form. The Zn1 ion is also coordinated by the imidazole groups from three different histidine residues (His99, His101, and His162), while Zn2 is coordinated by Asp103, Cys181, His223, and one water molecule (Wat2). A similar arrangement of zinc−ligand structures was observed in other crystal structures in the presence of inhibitors (*15*, *16*), although the coordination of the water molecules is notably different in the structure at pH 9.0 reported by Carfi et al. (*14*).

X-ray data analyses have provided further structural details. For example, the presence of a buried Na^+ counterion, which is only 6 Å away from Zn2, has been postulated to contribute to the formation of the observed architecture of the coordination environment of the Zn ions. Interestingly, this buried Na^+ ion has not been observed in the *B. cereus* enzyme in which a positively charged arginine residue is projected toward the Zn2 site (the equivalent residue in *B. fragilis* is Cys104). It has been noted (*13*) that the position of the internal Na^+ ion could be a magnesium or calcium binding site under physiological conditions. On the other hand, crystallographic temperature factors, as well as the absence of charge density for some residues, suggest that a flexible loop composed of 11 residues (45−55) in the proximity of the active site could be important for substrate binding. In agreement with this, NMR experiments in aqueous solution have shown that the position of this flexible loop, which evolves dynamically as a typical β-hairpin loop, is altered upon ligation of a thiol−ester compound which is a tight inhibitor (*17*, *18*). Thus, it has been proposed that the plasticity of the β-hairpin loop could be a necessary and underlying determinant for full catalytic activity (*18*).

In an effort to evaluate the roles of several conserved residues in binding and catalysis, site-directed mutants have been generated and characterized (*19*−*22*). As expected, the most remarkable effects resulted when the zinc-ligating residues were altered. For example, the Cys181Ser mutant binds only one zinc(II) ion, its catalytic activity being notably reduced (*19*, *21*). When the Asp103 residue was mutated to a neutral asparagine residue, the mutant enzyme binds one (29%) or two (71%) zinc ions and exhibits catalytic activities reduced by factors of $\sim^1/_2$ and $\sim^1/_{25}$ for benzylpenicillin and imipenem, respectively, as substrates (*21*). The Asp103Ser and Asp103Cys mutants bind the same amount of zinc(II) as the wild-type *B. fragilis* enzyme; however, 10^5- and 10^2-fold decreases in activity against nitrocefin are observed, respectively (*20*). Mutation of Asp103 into the hydrophobic residue Val results in a mutant that binds less than one zinc ion on average and exhibits a k_{cat} that is $\sim 10^4$-fold lower than that of the wild type for the hydrolysis of nitrocefin (*23*). Substitution of the nearby Cys104 residue with an arginine also affects catalysis (*22*). The mutant enzyme has the ability to bind 1 or 2 equiv of zinc as the *B. cereus* enzyme. Indeed, the Cys104Arg mutation of the *B. fragilis* enzyme as well as the removal of 1 equiv of zinc mimics what occurs in the mononuclear *B. cereus* enzyme. Kinetic measurements indicate that the catalytic efficiency of the Cys104Arg mutant decreases significantly in either its mononuclear or dinuclear form, approximating many of the mechanistic features of the *B. cereus* enzyme. This result contrasts with former reports that the catalytic efficiency of the dinuclear enzymes is only marginally superior to that of the mononuclear forms (*24*, *25*).

Very recently, a molecular dynamics (MD) simulation of the *B. fragilis* system has been reported (*26*). In this work, two different models for inhibitor binding to the *B. fragilis* enzyme were determined and compared with the structural and motional characteristics of the unbound protein in solution. These MD simulations have revealed a slight increase in the overall rigidity of the protein upon inhibitor binding, in agreement with the NMR NOE experimental results. However, in the simulation of the unbound form of the enzyme, the reported data concerning the structure and flexibility of the zinc environments were limited to what was necessary to build the model system (*26*).

In a previous quantum mechanical (QM) study (*27*), we investigated several cluster systems representing the coordination of the zinc ions in the active site of the metallo-β-lactamases. A $[Zn_2(\mu\text{-OH})(\text{methylimidazole})_4(SCH_3)(CH_3\text{-}COOH)]^{2+}(H_2O)$ cluster model reproduces the four and five coordination around Zn1 and Zn2, respectively, as observed crystallographically. The bridging hydroxide and the acetate moiety were bound through a Zn1−O···HOOC−Zn2 hydrogen bond, while the Zn2···OH_2 interaction was much weaker than the rest of the zinc−ligand bonds. When the model system had a global charge of +1 after deprotonation of the acetate ligand, the bridging hydroxide also establishes a Zn1−OH···OOC−Zn2 contact while the water molecule is placed in the second solvation shell around the Zn2 ion. Interestingly, the gas-phase basicity of the Zn1−OH···OOC−Zn2 interaction was found to be ∼20 kcal/mol higher than that of a zinc-bound hydroxide in a $[Zn(\text{methylimidazole})_3(OH)]^+$ complex, and therefore, a high pK_a could be possible. Unfortunately, very high levels of theory are required to accurately predict absolute pK_as for the metal complexes because small errors in the gas-phase energies or in solvation free energies can lead to very large errors on an absolute pK_a scale. On the other hand, it was also found that open configurations in which the hydroxide bridge between the zinc ions is lost have an intrinsic stability that is similar to those of the bridged configurations ($\Delta E \sim 1-2$ kcal/mol). A similar result was also obtained in a QM study on metallolactamase cluster models, including some water molecules in the second solvation shell around Zn2 (*28*). Therefore, all these calculations indicate that the zinc centers in the zinc β-lactamases could be linked through a *labile* Zn1−OH−Zn2 bridge.

Clearly, a theoretical description of the structure and dynamics of the unbound form of the dinuclear *B. fragilis* enzyme would be useful in further understanding substrate−inhibitor binding and the reaction mechanism. As a continuation of our previous work (*27*), we have studied the structural and energetic influences of the enzymatic environment on the relative stability of different dizinc rearrangements. This allows us to find out which cluster models are the most adequate representation of the actual coordination polyhedrons of the zinc ions in the enzyme. In this article, we focus on the flexibility of the Zn1−OH−Zn2 hydroxide bridge in the *B. fragilis* enzyme. First, we present QM optimizations of cluster systems at the HF/6-31G*, B3LYP/6-31G*, and PM3 levels of theory. Subsequently, molecular dynamics (MD) simulations of the fully solvated *B. fragilis*

Scheme 1

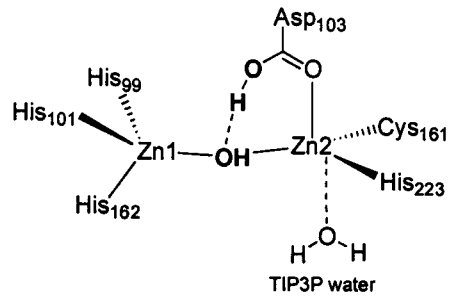

A(Asp-COOH)

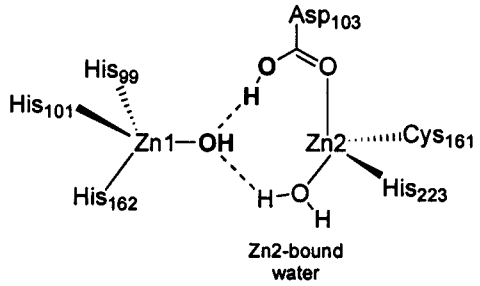

B(Asp-COOH)

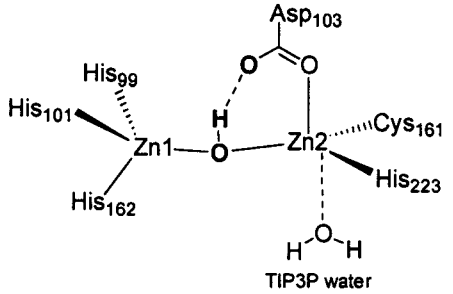

A(Asp-COO)

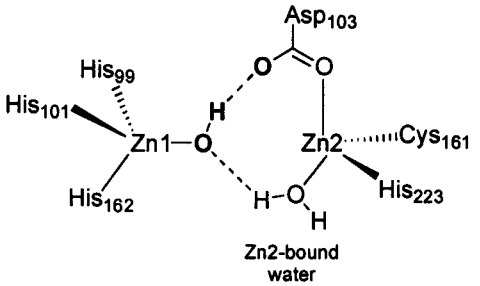

B(Asp-COO)

enzyme are performed assuming four different configurations of the active site as shown in Scheme 1. The **A(Asp-COO)** and **A(Asp-COOH)** models, which differ only in the protonation state of Asp103, represent the "tight" or the "Zn1−OH−Zn2 bridged" configurations in which a tetrahedron (Zn1) and a trigonal pyramid (Zn2) share the common hydroxide ligand. The **B(Asp-COO)** and **B(Asp-COOH)** models correspond to "loose" or "nonbridged" configurations which lack the Zn1−OH−Zn2 bridge. In these loose configurations, one water molecule binds directly to Zn2 and both zinc ions have stable tetrahedral coordination environments. In addition, the influence of the buried sodium ion near the Zn2 position was investigated by carrying out a secondary MD simulation of the **A(Asp-COOH)** model after replacing the sodium ion with an internal water molecule [this simulation will be labeled as **A(Asp-COOH)-noNa**$^+$]. The analyses of the MD trajectories allowed us to characterize interactions between the important functional groups that could play a role in catalysis or substrate binding. Also of particular interest are water molecules in the active site that cross-link important residues and the dynamics of the active site β-hairpin loop. The relative stabilities of the different MD configurations were analyzed by performing QM/MM optimizations of the dizinc clusters embedded in the protein followed by linear scaling QM calculations on protein subsystems. The PM3 semiempirical Hamiltonian and the Divide and Conquer approach (*29*, *30*) were adopted in the linear scaling QM calculations, while solvent effects were included by means of a continuum model.

COMPUTATIONAL METHODS

Gas-Phase QM Calculations. We explored the potential energy surface (PES) of cluster systems relevant to the enzyme configurations at the HF/3-21G*, HF/6-31G*, and B3LYP/6-31G* levels of theory (*31*−*33*). Although the HF/3-21G* results are not presented herein, HF/3-21G* analytical frequency calculations were carried out to characterize the nature of the critical points on the PES.

All the QM calculations were carried out in the gas phase using the Gaussian 98 suite of programs (*34*). Geometry optimizations were carried out with no constraints using Schlegel's algorithm and redundant internal coordinates. To locate transition structures on the gas-phase PES connecting the tight and loose structures, we employed the synchronous transit-guided quasi-Newton method (STQN) implemented in Gaussian98. Atomic charges were computed for all the structures according to the natural population analysis scheme (*35*).

The HF/6-31G* and B3LYP/6-31G* structures and energies were compared with those obtained from semiempirical calculations using the PM3 Hamiltonian (*36*) to test the ability of the semiempirical methods to reproduce the energies and structures of the dizinc complexes. Throughout this work, we employed a new PM3 parametrization for zinc, which has been obtained using a genetic algorithm in our laboratory. The parametrization reference set, which utilized the thermochemical data used to obtain the original PM3 parameters (*37*), was augmented with structural and energetic data obtained from ab initio model systems of zinc enzymes and other zinc complexes (*38*). The DivCon program was used to carry out the PM3 QM calculations (*39*).

Molecular Mechanics Parametrization of the Zinc Environments. As in our previous work on the *B. cereus* enzyme (*40*), we adopted the bonded approach for the metal ion representation which involves placing explicit bonds between the zinc cation and its surrounding environment (*41*, *42*).

We note, however, that in the **A(Asp-COOH)** and **A(Asp-COO)** configurations, the Zn2-bound water molecule observed in the initial X-ray structure is described as a TIP3P water molecule (i.e., no Zn2−water force constant was included in the force field representation), whereas Wat2 is explicitly bound to Zn2 in the **B(Asp-COOH)** and **B(Asp-COO)** models. This is in agreement with QM calculations showing that the Zn2···water interaction has a much weaker character in the tight cluster models than in the loose ones (see below). This approach differs from that followed by Salsbury et al. (*26*) in which only the protein ligands are covalently bound to the zinc ions whereas all the zinc−water interactions were represented by nonbonded forces. The MM parameters and further details about the parametrization procedure are reported in the Supporting Information.

MD Simulations. The coordinates of the protein atoms were taken from molecule A in the *B. fragilis* 1.85 Å crystal structure of Concha et al. (PDB entry 1ZNB) (*13*). In this high-resolution structure, coordinates were not available for the Trp49 and Gly48 residues due to the lack of observed density. The initial geometry for these residues was therefore built by molecular modeling using the rest of the protein as a template. The resultant structure, as well as the crystallographic water molecules, was surrounded by a periodic box of TIP3P water molecules which extend ∼10 Å from the protein atoms. This resulted in a protein system (∼3500 atoms) being solvated by 240 X-ray water molecules and ∼12200 additional water molecules. All of the ionizable residues were set to their pH 7 protonation states except the Zn2-bound Asp103 residue in the **A(Asp-COOH)** and **B-(Asp-COOH)** configurations. In addition to the crystallographic Na^+ ion close to Zn2, five (in the **Asp-COOH** models) or six (**Asp-COO**) Na^+ counterions were placed 20 Å beyond the zinc atoms to neutralize the models using LEaP (*43*). The parm96 version of the all-atom AMBER force field was used to represent the protein system (*44*).

To remove bad contacts in the initial geometry, energy minimization was carried out using a conjugate gradient minimizer (2500 steps for the water molecules followed by 2500 steps for the whole system). MD simulations were carried out using the SANDER program included in version 5.0 of the AMBER package (*45*). The time step was chosen to be 1.5 fs, and the SHAKE algorithm (*46*) was used to constrain all bonds involving hydrogen atoms. A nonbond pairlist cutoff of 10.0 Å was used, and the nonbonded pairlist was updated every 25 time steps (*47*). The pressure (1 atm) and the temperature (300 K) of the system were controlled during the MD simulations by Berendsen's method (*48*) (a separate scaling factor for the solute and the solvent temperatures was used). Periodic boundary conditions were applied to simulate a continuous system (*47*). To include the contributions of long-range interactions, the Particle−Mesh−Ewald (PME) method (*49*) was used with a grid size of 64 × 64 × 64 (grid spacing of ∼1 Å) combined with a fourth-order *B*-spline interpolation to compute the potential and forces between grid points. The estimated root-mean-square deviations of the PME force errors (*50*) were lower than 10^{-4} during the simulations.

For the **A(Asp-COO)**, **A(Asp-COOH)**, and **A(Asp-COOH)-noNa$^+$** configurations, an equilibration period of 200 ps resulted in a protein system sufficiently adjusted to its solvent environment according to the convergence of the dimensions of the simulation box and the evolution of the trajectories. Subsequently, for each configuration, a 1 ns trajectory was computed and coordinates were saved for analyses every 50 time steps. The 0.2 ns instantaneous structures of the **A(Asp-COO)** and **A(Asp-COOH)** systems were adopted as the starting structures for the **B(Asp-COO)** and **B(Asp-COOH)** systems, respectively. The zinc complexes in the active sites were converted manually into the loose configurations. All other water molecules were retained and placed in the **B(Asp-COO)** and **B(Asp-COOH)** systems, which were then reminimized for an additional 2500 steps. The MD simulation protocols for **B(Asp-COO)** and **B(Asp-COOH)** were identical to those for **A(Asp-COO)** and **A(Asp-COOH)**. For both trajectories, an equilibration period of 200 ps was followed by a 1 ns production run. All of the MD results were analyzed using the CARNAL module of AMBER 5.0 and some specific trajectory analysis software developed locally. Some figures were produced with the programs Molscript (*51*) and Raster3D (*52*).

QM/MM and Linear Scaling QM Calculations. For the **A(Asp-COO)**, **A(Asp-COOH)**, **B(Asp-COO)**, and **B(Asp-COOH)** configurations, a series of QM/MM minimizations were performed in which the dizinc complexes (QM region) were relaxed while the rest of the protein and a solvent cap of 1500 water molecules centered on the Zn1-bound oxygen atom (MM region) were held fixed. Initial geometries were taken from snapshots extracted every ∼10 ps during the simulations. In these calculations, the PM3 Hamiltonian augmented with the new set of parameters for zinc (*38*) was used to describe the zinc cations, the zinc-bound water molecules, and the side chains of liganding residues His99, His101, His162, Asp103, Cys181, and His223. The AMBER force field was used for the rest of the system. Hydrogen link atoms were placed at the corresponding Cβ atoms to cap exposed valence sites due to bonds which crossed the QM−MM boundary. The ROAR 2.0 program (*53*) was used to carry out the QM/MM minimizations.

From the QM/MM-relaxed structures, we selected subsystems formed by all residues within 12 Å of the Zn1-bound hydroxide, including all of the residues in the β-hairpin loop (∼1000 protein atoms). In addition, the water molecules around the buried Na^+ ion adjacent to the Zn2 site were also extracted. Terminal *N*-methylamine or acetyl groups were placed at the C and N backbone atoms of those residues cleaved from the protein main chain by the truncation process. Single-point PM3 calculations were performed on these *B. fragilis* subsystems using the Divide and Conquer (D&C) approach (*29*) in which incorporation of solvent effects within a QM methodology was accomplished by merging the D&C algorithm with the Poisson−Boltzmann equation (*54*). An additional "nonpolar" contribution to the solvation energy due to the creation of a solute cavity in the continuum is ascribed to a term proportional to the solvent accessible surface area of the solute. From these semiempirical calculations, we estimated the standard free energy *G* of each protein subsystem by combining the corresponding heat of formation of the protein part (H^0) with its solvation energy (ΔG^0_{solv}); that is, $G^0 \approx H^0 + \Delta G^0_{solv}$. The G^0 values were averaged along the ∼100 calculations that were performed for each of the active site configurations. Note, however, that entropic contributions due to protein flexibility are not included in the resultant *G* values.

The DivCon99 program (*39*) was employed to perform the D&C and D&C−PB PM3 calculations using the dual-buffer layer scheme (inner buffer layer of 4.0 Å and an outer buffer layer of 2.0 Å) with one protein residue per core. This D&C *subsetting* with a total buffer region of 6.0 Å gives generally accurate relative energies (*55*). A cutoff of 9.0 Å was used for the off-diagonal elements of the Fock, one-electron, and density matrices. The D&C−PB calculations were carried out using the computational protocol described in detail elsewhere (*54*).

RESULTS

QM Calculations on Cluster Models

Figures 1 and 2 display the optimized structures for the series of cluster models studied in this work, while Table 1 lists the most important interatomic distances at the different levels of theory. Structures **1(COOH)** and **1(COO)** correspond to the Zn1−OH−Zn2 bridged structures with Zn1−Zn2 distances of ∼3.5 Å, denoted as $\mathbf{5B_H}$ and **5**, respectively, by Díaz et al. (*27*) In the gas phase, **1(COOH)** and **1(COO)** are directly connected with the nonbridged structures **3(COOH)** and **3(COO)**, respectively, passing through saddle points $\mathbf{2_{TS}(COOH)}$ and $\mathbf{2_{TS}(COO)}$ whose transition vectors were dominated by the stretching of the Zn2···O(Wat1) bond according to HF/3-21G* frequency calculations ($\nu_{TS} \sim 40$ cm^{-1}).

We see in Figures 1 and 2 that, for both protonation states, the rupture of the Zn1−OH−Zn2 bridge determines the positioning of Wat2 in the first solvation shell around Zn2 showing Zn−O distances of ∼2.0 Å at **3(COOH)** and **3(COO)**. This water molecule was interacting weakly with Zn2 in **1(COOH)** (Zn2···O distance of ∼2.4 Å) or was located in the second solvation shell around Zn2 in **1(COO)** (Zn2···O distance of ∼3.9 Å). In the absence of shared ligands, both zinc ions lie ∼4.6−5.0 Å apart in separate tetrahedral cavities which are connected via two hydrogen bonding interactions between the Zn1-bound hydroxide and the Zn2−Wat2 and Zn2−COO(H) moieties.

The rupture of the Zn1−OH−Zn2 bridge is more favorable in the **COOH** protonation state than in **COO**. Since the Zn1 and Zn2 coordination spheres bear a similar global charge of approximately +1e in the **COOH** structures, increasing the Zn1−Zn2 separation results in a less repulsive distribution of charges in the gas phase. This explains why the **3(COOH)** structure is more stable than **1(COOH)** by 2.6 (HF) and 6.0 kcal/mol (B3LYP). In the **COO** models, the Zn2 ion and its ligands have a global charge of ∼0 whereas the Zn1 environment retains a positive charge of +1.0 as in the **COOH** models. Hence, the loss of the Zn1−OH−Zn2 bridge in the **COO** clusters is not compensated by a reduction in the level of repulsive electrostatic interactions, and therefore, the **3(COO)** structure is predicted to be less stable than **1(COO)** by 5.9 (HF) and 4.4 kcal/mol (B3LYP). The calculated energies for saddle points $\mathbf{2_{TS}(COOH)}$ and $\mathbf{2_{TS}(COO)}$ with respect to their precursors, **1(COOH)** and **1(COO)**, respectively, have values of 4 and 10 kcal/mol, respectively. These results indicate that the **COOH** dizinc complexes would preferentially favor the nonbridged form while the **COO** models prefer to retain the Zn1−OH−Zn2 bridge interaction. Nevertheless, the energy changes are relatively small, and consequently, the influence of the protein and solvent environment must be considered to discuss the relative stability of the configurations in the actual *B. fragilis* active site.

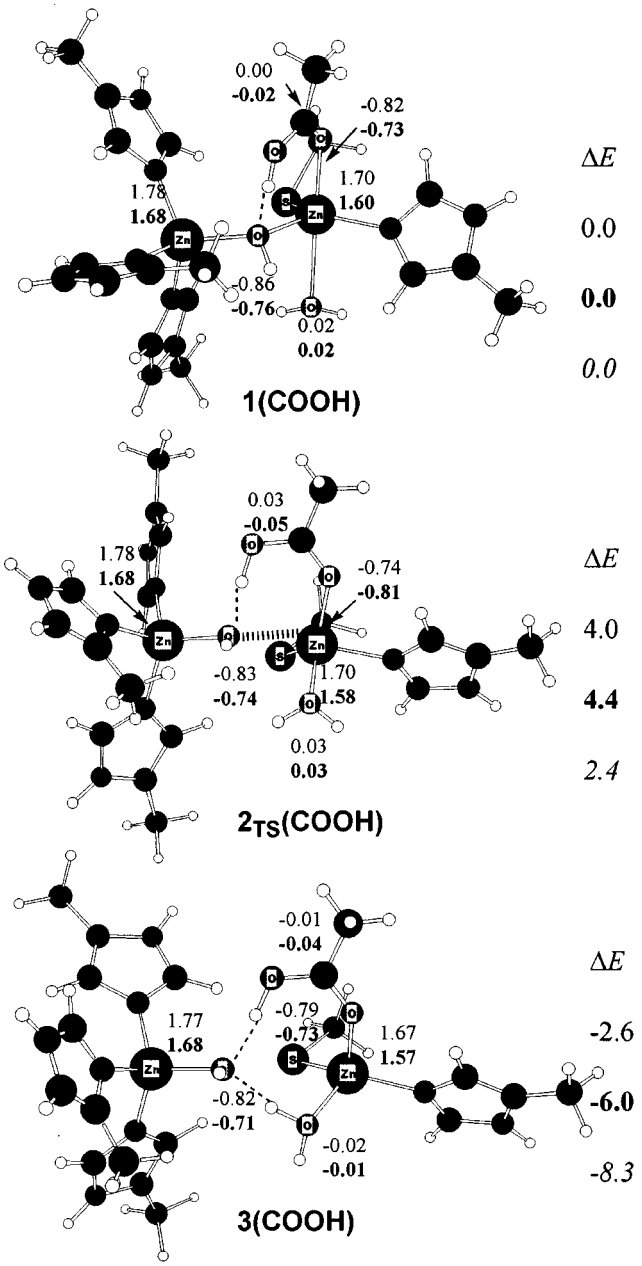

FIGURE 1: Optimized structures involved in the rupture of the Zn1−OH−Zn2 bridge in the **COOH** structures. NPA charges of the zinc ions and some zinc−ligand moieties are given at the HF/6-31G* and B3LYP/6-31G* (bold) levels of theory. Relative energies (kilocalories per mole) at the HF/6-31G*, B3LYP/6-31G* (bold), and PM3 (italic) levels of theory are also indicated.

These QM energy profiles also permit us to analyze the relative performance of the levels of theory employed to describe the dizinc complexes. In general, HF/6-31G* and B3LYP/6-31G* geometries around the Zn ions are quite similar, in agreement with previous observations (*27*, *56*). However, the charge transfer effects in the Zn1−OH···(H)-OOC−Zn2 and Zn1−HO···H_2O−Zn2 moieties are more important at the B3LYP/6-31G* level. For example, the B3LYP charges for Zn are ∼0.10e smaller than the HF ones. In addition, the strength of the O−H···O contacts is greater at the B3LYP/6-31G* level than at the HF/6-31G* level as

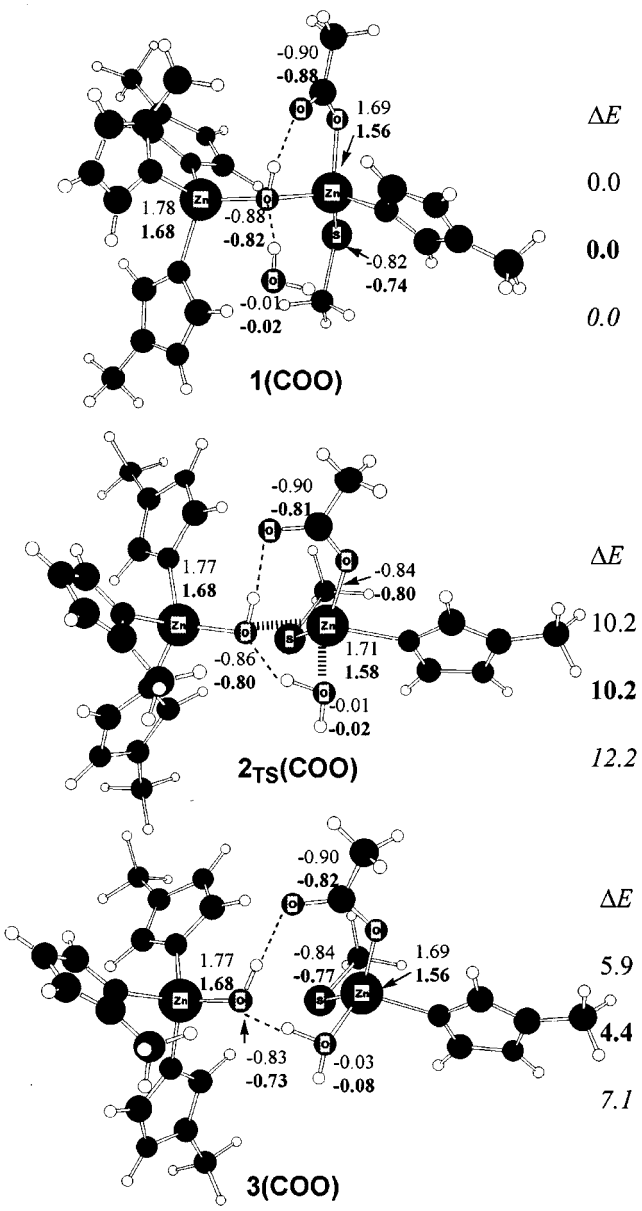

FIGURE 2: Optimized structures involved in the rupture of the Zn1−OH−Zn2 bridge in the **COO** structures. NPA charges of the zinc ions and some zinc−ligand moieties are given at the HF/6-31G* and B3LYP/6-31G* (bold) levels of theory. Relative energies (kilocalories per mole) at the HF/6-31G*, B3LYP/6-31G* (bold), and PM3 (italic) levels of theory are also indicated.

reflected in the shorter O−O distances when electron correlation is included. As a result, the nonbridged complexes, in which the Zn1 and Zn2 environments interact via two O−H···O contacts, are more stable at the B3LYP/6-31G* level than at the HF/6-31G* level.

Figures 1 and 2 as well as Table 1 also show energetic and structural data obtained using the semiempirical PM3 Hamiltonian. As mentioned in Computational Methods, a new set of PM3 parameters for Zn was used because the original PM3 parametrization gave poor results for the dinuclear complexes (e.g., the Zn2−carboxylate interaction was not stable). The PM3(Zn refined) level predicts Zn−ligand distances which are quite close to the HF/6-31G* ones except for the weak interaction between Zn2 and Wat2 in **1(COOH)** (see Table 1). Interestingly, the new PM3 parameters for Zn result in atomic charges of the zinc ions which are much more "realistic" (∼0.8e; Mulliken charges) than those obtained with the previous set of parameters (∼0.0e). The flexible behavior of the zinc complexes in interchanging between the bridged and nonbridged structures can also be described with the PM3(Zn refined) level which reproduces semiquantitatively the energetics of this process.

MD Simulations

As mentioned in the introductory section, we simulated the unbound form of the *B. fragilis* enzyme in five different configurations of the active site region: **A(Asp-COOH)**, **B(Asp-COOH)**, **A(Asp-COO)**, **B(Asp-COO)**, and **A(Asp-COOH)-noNa**$^+$ (see Scheme 1). While the **A** simulations assume the presence of a Zn1−OH−Zn2 bridge in the active site, the **B** models examine the corresponding nonbridged complexes. The neutral (**COOH**) and negatively charged (**COO**) protonation states of the Zn2 ligand Asp103 were considered in these simulations.

We will first present the results of the MD simulations for the series of models **A(Asp-COOH)**, **B(Asp-COOH)**, **A(Asp-COO)**, and **B(Asp-COO)**. Then the impact on the enzyme dynamics and structure, caused by the removal of the buried Na^+ ion, will be analyzed by means of the **A(Asp-COOH)-noNa**$^+$ simulation.

RMSD and RMSF Values. The heavy atom root-mean-square deviations (rmsds) of the simulated zinc β-lactamase protein relative to the 1ZNB crystal structure are given in Table 2. In all the simulations, the rmsd value was, on average, ∼1.5 Å except for that of the **B(Asp-COOH)** configuration which had a slightly greater rmsd value of ∼1.7 Å. Figures S8−S12 in the Supporting Information show the time evolution of the rms deviation of the instantaneous structures from the 1ZNB crystal structure for the different protein configurations. In these plots, the maximum instantaneous deviations in the rmsd profiles with respect to their mean values were not large, approximately ±0.2 Å. The largest deviations observed in the rsmd profiles can be traced to the movements of the protein loops and the solvent-exposed α-helixes. In particular, the β-hairpin loop of residues 41−55, the extended loop bordering the active site (residues 182−196), and the terminal α-helix in the C-domain present the largest deviations as observed when the average protein structure from the different simulations are superposed upon the initial X-ray structure (see Figure S13 in the Supporting Information). Globally, the structural changes in the protein were not large over time, and therefore, we concluded that the different models evolved in an equilibrium state with respect to the rms deviations during the course of the simulations.

The rms flexibility (rmsf) of the whole protein was calculated by comparing the instantaneous protein structure to the average one (see Table 3). The calculated rmsf values for the entire protein in the **A(Asp-COOH)**, **A(Asp-COO)**, and **B(Asp-COO)** models had values of 0.98, 0.88, and 0.95 Å, respectively. The corresponding rmsf values for the backbone atoms (0.81, 0.66, and 0.74 Å) were close to the all-atom ones, demonstrating the importance of backbone motion. Note that the **A(Asp-COOH)** state is more flexible than **A(Asp-COO)**. The largest protein flexibility corresponds to the **B(Asp-COOH)** model (protein rmsf = 1.16 Å), in consonance with its larger rms deviations relative to

Table 1: HF/6-31G*, B3LYP/6-31G* (bold), and PM3 (italic) Interatomic Distances in Angstroms for the Series of Dizinc Clusters Studied in This Work

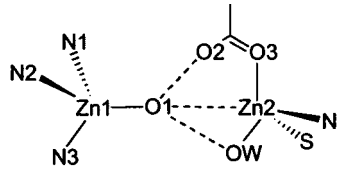

Atom numbering

	Zn1−Zn2	Zn1−N1	Zn1−N2	Zn1−N3	Zn1−O1	Zn2−O1	Zn2−O3	Zn2−S	Zn2−N	Zn2−OW	O1−OW	O2−O1
	3.53	2.05	2.10	2.07	1.97	2.06	2.19	2.31	2.07	2.41	2.94	2.73
1(COOH)	**3.55**	**2.00**	**2.04**	**2.03**	**1.97**	**2.06**	**2.15**	**2.27**	**2.03**	**2.41**	**2.83**	**2.63**
	3.51	*2.04*	*2.08*	*2.05*	*1.97*	*1.96*	*1.96*	*2.50*	*2.05*	*2.93*	*3.15*	*2.75*
	4.33	2.06	2.11	2.07	1.93	2.89	2.02	2.29	2.08	2.12	2.92	2.58
2(COOH)	**3.55**	**2.00**	**2.04**	**2.03**	**1.97**	**2.06**	**2.15**	**2.27**	**2.03**	**2.41**	**2.83**	**2.54**
	4.71	*2.03*	*2.08*	*2.06*	*1.87*	*3.13*	*1.87*	*2.46*	*2.04*	*2.09*	*3.17*	*2.66*
	5.03	2.05	2.08	2.06	1.94	3.70	2.05	2.28	2.02	2.00	2.66	2.67
3(COOH)	**5.01**	**2.01**	**2.03**	**2.02**	**1.95**	**3.58**	**2.02**	**2.26**	**1.98**	**2.04**	**2.60**	**2.60**
	5.14	*2.04*	*2.08*	*2.06*	*1.89*	*3.73*	*1.88*	*2.46*	*2.02*	*2.00*	*2.68*	*2.67*
	3.54	2.06	2.09	2.07	1.93	2.04	1.97	2.32	2.09	3.95	2.82	2.81
1(COO)	**3.50**	**2.02**	**2.04**	**2.03**	**1.92**	**2.02**	**1.98**	**2.27**	**2.05**	**3.89**	**2.73**	**2.68**
	3.59	*2.04*	*2.10*	*2.08*	*1.99*	*2.04*	*1.97*	*2.38*	*2.08*	*4.28*	*2.77*	*2.72*
	3.99	2.06	2.13	2.08	1.88	2.58	1.95	2.34	2.14	2.13	2.56	2.86
2(COO)	**3.78**	**2.02**	**2.08**	**2.03**	**1.89**	**2.40**	**1.96**	**2.31**	**2.10**	**2.14**	**2.51**	**2.72**
	3.97	*2.08*	*2.12*	*2.04*	*1.86*	*2.49*	*1.87*	*2.54*	*2.08*	*2.08*	*2.53*	*2.73*
	4.91	2.06	2.10	2.08	1.88	3.78	1.94	2.33	2.09	2.06	2.58	2.99
3(COO)	**4.64**	**2.01**	**2.05**	**2.03**	**1.88**	**3.55**	**1.94**	**2.29**	**2.04**	**2.01**	**2.48**	**2.80**
	4.96	*2.08*	*2.10*	*2.05*	*1.83*	*3.63*	*1.86*	*2.52*	*2.05*	*1.99*	*2.54*	*2.79*

Table 2: Summary of the rms Deviations and Radii of Gyration

model	rmsd (Å) for protein	rmsd (Å) for backbone	rad_{gyr} (Å)[a]
A(Asp-COOH)	1.48 ± 0.14	1.09 ± 0.12	16.94 ± 0.10
B(Asp-COOH)	1.69 ± 0.11	1.35 ± 0.15	17.00 ± 0.16
A(Asp-COO)	1.52 ± 0.10	1.16 ± 0.10	17.00 ± 0.15
B(Asp-COO)	1.49 ± 0.10	1.09 ± 0.12	16.93 ± 0.16
A(Asp-COOH)-noNa$^+$	1.56 ± 0.12	1.23 ± 0.11	17.05 ± 0.16

[a] X-ray value of 16.77 Å.

the crystal structure. As expected, the protein loops and the external α-helixes are more flexible on average than the inner core of the protein formed by the twisted β-sandwich.

Structure of the Dizinc Complexes. Typical snapshots of the active site region and schematic representations of the most important contacts observed during the MD simulations are shown in Figure 3 [**A(Asp-COOH)** and **B(Asp-COOH)** models] and in Figure 4 [**A(Asp-COO)** and **B(Asp-COO)**]. The geometrical fluctuations observed during the MD simulations gave us extensive insight into the structural influence of the protein and water environment on the dizinc complexes that were previously studied in the gas phase.

For the **A(Asp-COOH)** simulation, the most important distances that characterize the active site region (that were not explicitly included in the force field representation) were found to be in excellent agreement with those obtained from the 1ZNB X-ray crystal structure (*13*). For example, the Zn1−Zn2 separation was 3.5 Å, while the Zn2 ion is 6.0 Å away from the buried Na^+ cation on average. Interestingly, the Zn2 cation interacts with a TIP3P water molecule throughout the MD simulation with a Zn2−OW distance of ∼2.2 Å (see below). In the case of the **A(Asp-COO)** simulation, both zinc ions maintain their tetrahedral coordination which resulted from the QM gas-phase calculations. However, the protein−solvent environment reduces the average Zn1−Zn2 separation (3.3 Å) and simultaneously accentuates the tetrahedral coordination around the Zn2 site with respect to the QM cluster model **1(COO)**. In **A(Asp-COO)**, the Asp103 carboxylate group has an asymmetrical bidentate coordination to Zn2, with mean Zn−O distances of 1.9 and 2.9 Å (see Figure 4).

In the nonbridged configuration, **B(Asp-COOH)**, the separate tetrahedral environments of the Zn1 and Zn2 ions were stable all along the computed trajectory. The mean value for the Zn1−Zn2 distance was 4.44 Å. As expected, the loss of the Zn1−OH−Zn2 bridge reduces the Zn2−Na^+ separation to 5.6 Å on average. Interestingly, the Zn1−HO···HOOC−Zn2 and Zn1−HO···H_2O−Zn2 hydrogen bonds were preserved during the entire **B(Asp-COOH)** simulation, suggesting that this mode of binding could be dynamically stable.

In the case of the **B(Asp-COO)** model, the mean Zn1−Zn2 separation was 4.02 Å, only 0.7 Å longer than that observed for **A(Asp-COO)**. This suggests that the protein and solvent environment restricts the flexibility of the Zn1−OH−Zn2 bridge when Asp103 is unprotonated. In contrast with the **B(Asp-COOH)** model, the contacts between the Zn1 and Zn2 coordination spheres can fluctuate more readily. For example, the Zn1−OH moiety and the Zn2-bound Wat2 molecule changed from a direct H-bond contact into a water-mediated interaction in the second half of the **B(Asp-COO)** trajectory. Simultaneously, the carboxylate group of the Glu47 residue, which is located in the active site β-harpin loop, forms a salt bridge with the Zn2 environment mediated by the Zn2-bound water molecule (see Figure 4b). The Glu47 carboxylate group in the **B(Asp-COO)** state can also interact with the Zn1-bound hydroxide through the intermediacy of bulk water molecules.

Coordination Geometry of the Buried Na^+ Ion. The sodium ion close to the Zn2 ion has a trigonal bypyramidal

Table 3: Summary of the rms Fluctuations (Å)

model	protein	backbone	α-helixes	β-strands	loops	β-hairpin loop (residues 45−51)	extended loop (residues 182−198)
A(Asp-COOH)	0.98 ± 0.09	0.81 ± 0.11	0.85 ± 0.07	0.69 ± 0.05	0.99 ± 0.10	0.69 ± 0.11	0.97 ± 0.12
B(Asp-COOH)	1.16 ± 0.06	1.00 ± 0.07	1.09 ± 0.07	0.92 ± 0.06	1.11 ± 0.08	0.80 ± 0.12	0.96 ± 0.12
A(Asp-COO)	0.88 ± 0.08	0.66 ± 0.07	0.77 ± 0.07	0.70 ± 0.07	0.93 ± 0.12	1.03 ± 0.20	0.87 ± 0.17
B(Asp-COO)	0.95 ± 0.08	0.74 ± 0.08	0.83 ± 0.08	0.72 ± 0.07	1.07 ± 0.13	1.45 ± 0.24	0.78 ± 0.11
A(Asp-COOH)-noNa$^+$	0.98 ± 0.13	0.76 ± 0.12	0.78 ± 0.08	0.71 ± 0.08	1.13 ± 0.26	1.11 ± 0.22	0.77 ± 0.12

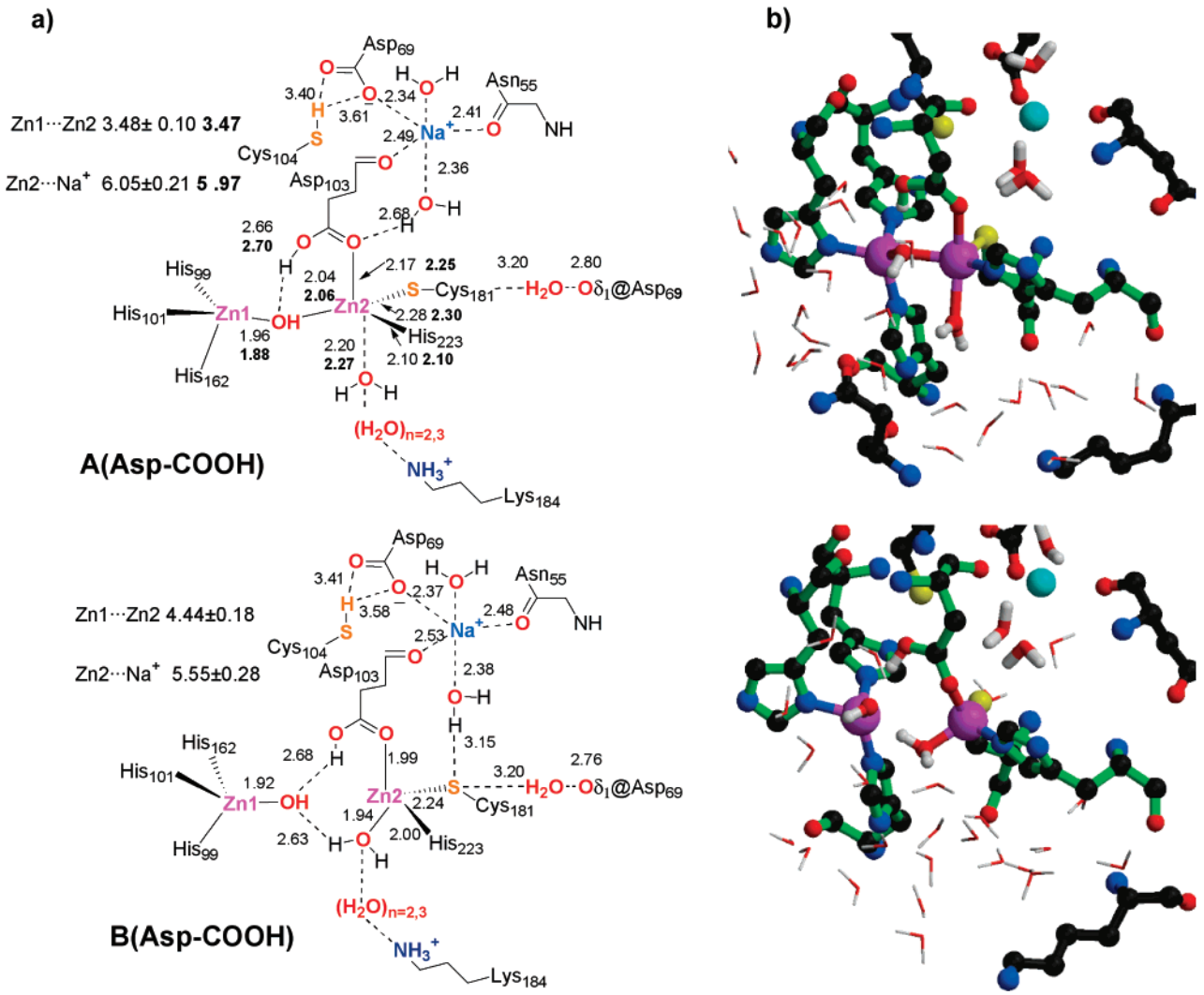

FIGURE 3: (a) Schematic representation of the most important interactions characterizing the active site of the **A(Asp-COOH)** and **B(Asp-COOH)** models. Some average distances between heavy atoms are given in angstroms (bold values correspond to X-ray values from the 1ZNB structure). (b) Snapshot of the active site in the **A(Asp-COOH)** and **B(Asp-COOH)** models.

coordination geometry. In the available X-ray structures, the sodium ligands are all oxygen atoms with average distances of 2.4 Å. The equatorial positions are occupied by Oδ1@Asp69, O@Asp103, and O@Asn55, while two buried water molecules occupy the axial positions. In all the simulations, the five coordination of the buried Na^+ remained stable, the mean values of the Na^+−oxygen distances being ∼2.4 Å as seen in the crystal structures (see Figures 3 and 4). The separation between Na^+ and Zn2 depends on the actual configuration of the dizinc complex with average values varying from 5.4 to 6.0 Å. The Zn2 and Na^+ environments interact through a Na^+···(OH_2)···Oδ1@Asp103−Zn2 contact in three of the examined trajectories [**A(Asp-COOH)**, **A(Asp-COO)**, and **B(Asp-COO)**] or a Na^+···(OH_2)···Sγ@Cys181−Zn2 contact in the **B(Asp-COOH)** model. Thus, in the models with the neutral Asp103, the Na^+···(OH_2)···Asp103 contact can readily change into a Na^+···(OH_2)···Cys181 contact as a consequence of the interchange between the **A** and **B** configurations of the active site. In the models with the negatively charged Asp103, the carboxylate group of Asp103 and the internal sodium are more tightly bound through a single water bridge.

Asp69 and Cys104. Asp69 is a conserved residue in the metallo-β-lactamases (Asp56 in the *B. cereus* numbering), which has a φ angle outside the allowed range (∼79° in the initial X-ray structure). This residue contributes to the binding of the internal sodium ion through a long-lived Oδ2···Na^+ contact (the equivalent interaction in *B. cereus* is an Asp56···Arg91 salt bridge). All the *B. fragilis* models reproduce the strained main chain conformation of Asp69,

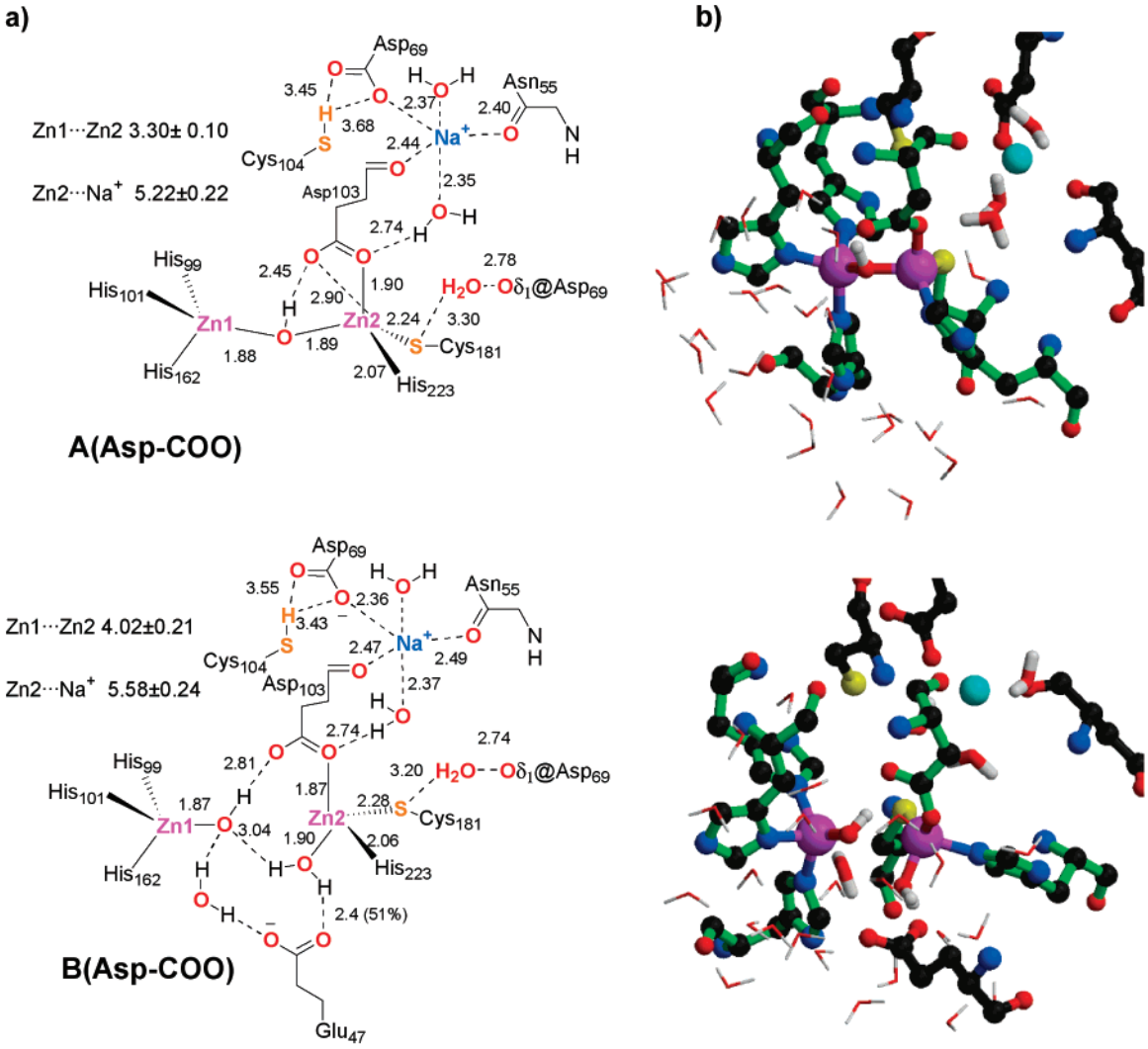

FIGURE 4: (a) Schematic representation of the most important interactions characterizing the active site of the **A(Asp-COO)** and **B(Asp-COO)** models. Some average distances between heavy atoms are given in angstroms. (b) Snapshot of the active site in the **A(Asp-COO)** and **B(Asp-COO)** models.

giving a φ angle average of $\sim 62 \pm 9°$ along the analyzed trajectories. In all of the simulations, the Oδ1@Asp69 atom is hydrated by a buried water molecule which acts as double proton donor by establishing a second long-lived H-bond with the Sγ atom of the Zn2-bound Cys181 residue. In addition, the carboyxlate group of Asp69 interacts with the thiol group of Cys104 by means of an asymmetric bifurcated hydrogen bonding interaction with the following average distances between heavy atoms: Sγ···Oδ1, ~3.4 Å; and Sγ···Oδ2, ~3.6−3.7 Å (see Figures 3 and 4). This is the only contact that stabilizes the polar side chain of Cys104, which is buried underneath the zinc centers. The fact that the network of interactions interconnecting Cys104, Asp69, the internal Na^+, and the Zn2-bound residues, Asp103 and Cys181, is highly stable in all four simulations confirms that these contacts can be crucial for the enzyme structure regardless of the actual protonation state and flexibility of the dizinc complexes in the active site.

Hydrophobic Pocket. According to rigid docking analyses (*13*), the side chains of Ala44, Ile46, Val52, and Ile72 form a hydrophobic pocket that is properly oriented to accommodate the aromatic portions of the acylamino side chains of penicillins and cephalosporins. Residues Val52 and Ile46 are at opposite ends of the active site β-hairpin loop, while Ile72 lies in a solvent accessible turn close to the internal Na^+ ion. We geometrically characterized the clustering of the Val52···Ile46···Ile72 residues on the basis of distances involving the center of mass of their side chains (see Table 4). According to our simulations, the relative conformation of these residues was largely dependent on the active site configuration. In fact, the bulky side chains of the three residues formed a clearly stable hydrophobic pocket only in the **A(Asp-COOH)** simulation. For the other configurations, the hydrophobic side chain of Ile46 pairs with only one residue, Val52 or Ile72.

Table 4: Summary of the Significant Distances (Å) of Hydrophobic Residues Ile46, Val52, and Ile72

model	side chain@Val52···side chain@Ile46	side chain@Ile46···side chain@Ile72
A(Asp-COOH)	5.36 ± 0.56	4.89 ± 0.36
B(Asp-COOH)	7.02 ± 1.38	5.98 ± 0.83
A(Asp-COO)	5.61 ± 0.47	5.46 ± 0.39
B(Asp-COO)	5.35 ± 0.75	6.98 ± 1.47
A(Asp-COOH)-noNa^+	6.59 ± 1.48	5.48 ± 0.61

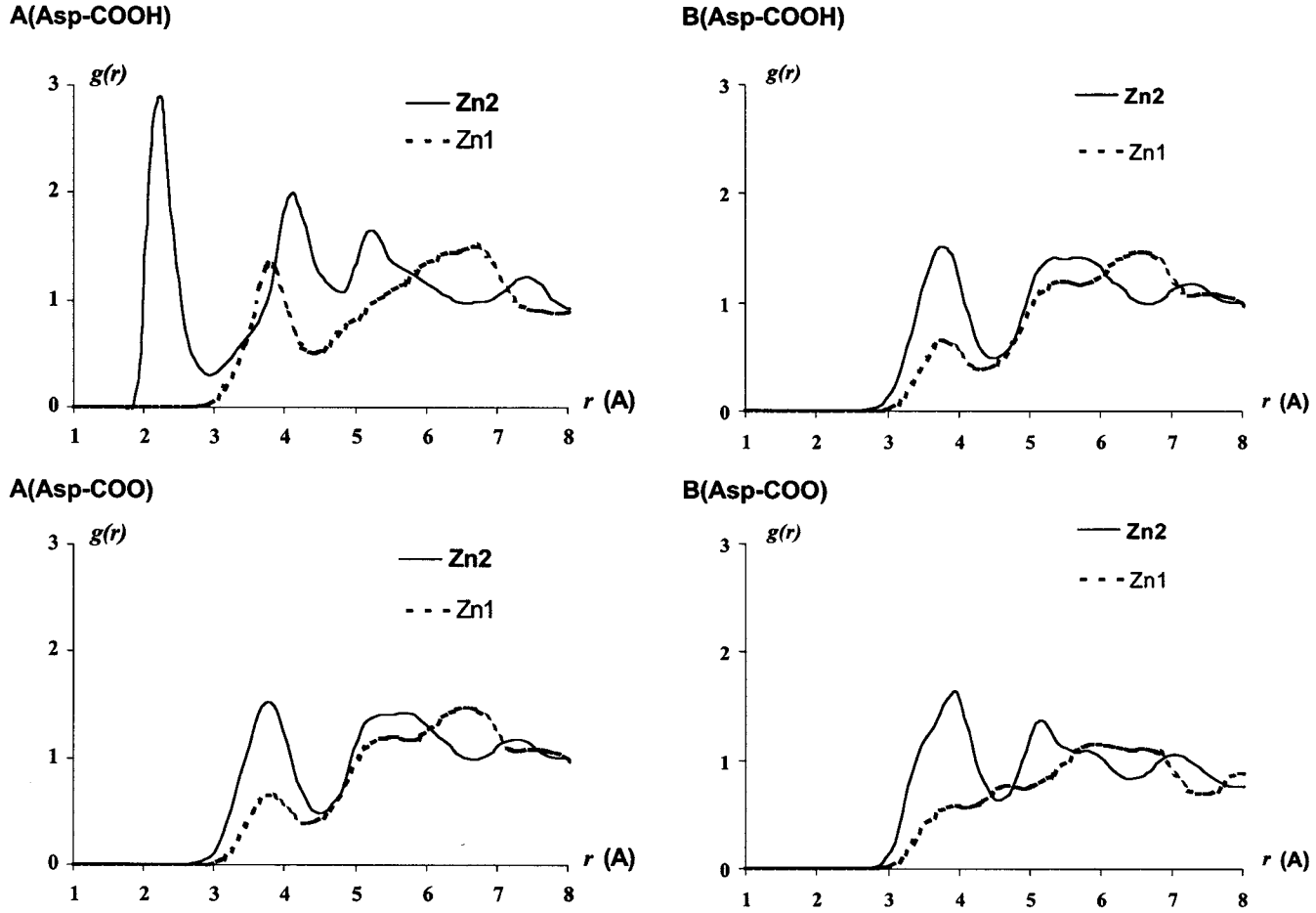

FIGURE 5: Atomic radial distribution function $g(r)$ for the zinc ions to the oxygens in the surrounding water molecules.

Solvation of the Zinc Ions. We initially characterized the solvation of the zinc ions by calculating the pair distribution functions $g(r)$ around the Zn1 and Zn2 ions to the water oxygen atoms in the surrounding TIP3P water molecules. Plots of the $g(r)$ functions as calculated from the different MD simulations are shown in Figure 5.

The $g(r)$ function for the Zn1 ion in the all the models reveals the presence of approximately two solvation layers centered at distances of ~3.8 and 6.5 Å, respectively. For the **B(Asp-COOH)**, **A(Asp-COO)**, and **B(Asp-COO)** models, the first peak has integrated values of 1.1, 1.3, and 0.7, respectively, that can be attributed to a water molecule solvating the Zn1-bound hydroxide. In the **A(Asp-COOH)** model, there is one more water molecule located ~4 Å from Zn1 which in turn hydrates the Zn2 ion. The second peak in the $g(r)$ function for Zn1 at larger distances mainly represents the solvation of the Zn1 ligands.

Hydration of the Zn2 site is of particular interest since a Zn2-bound water molecule has been proposed to be important in either substrate binding or catalysis in metallo-β-lactamases (*13*, *20*, *57*). Interestingly, the $g(r)$ plots around Zn2 obtained for the **A(Asp-COOH)** and **A(Asp-COO)** models are quite different. On one hand, the $g(r)$ function around Zn2 in the **A(Asp-COOH)** model has a sharp peak centered at 2.20 Å with an integrated value of 0.93, corresponding to the presence of a water bound to Zn2. In our simulation, the observed residence time for this water molecule ranged from ~100 to ~500 ps. On the other hand, the Zn2 position lacks a first hydration layer throughout the **A(Asp-COO)** simulations (see Figure 5). This suggests that the existence of a well-defined Zn2-bound water molecule (but freely interchangeable with bulk water) could be linked to the localization of a positive charge in the *B. fragilis* active site as present in the **A(Asp-COOH)** model. For the **B(Asp-COOH)** and **B(Asp-COO)** models in which the Zn2 ion is explicitly bound to the water molecule [this water is not considered in the $g(r)$ plots; thus, the first peak is absent], the $g(r)$ plots reveal the presence of a second solvation layer for Zn2 centered at ~5 Å that can be attributed to the water molecules in the first solvation shell of the Zn2−Wat2 molecule and the Oδ atoms of Asp104.

At this point, it is interesting to critically examine our results for the solvation of the Zn2 site. The force field used in the MD simulations represents two extreme situations: either nonbonded interactions between the Zn2 ion and the surrounding TIP3P molecules as in the **A(Asp-COOH)** and **A(Asp-COO)** trajectories or donor−acceptor H_2O−Zn2 interactions represented by an explicit force constant in the nonbridged **B(Asp-COOH)** and **B(Asp-COO)** models. However, we found in previous theoretical work (*58*) that zinc−water interactions are governed by a delicate balance between *hard*-like electrostatic forces and *soft*-like charge transfer interactions for which a simple MM representation might not fully account.

Other water molecules relatively close to the zinc atom constitute the first solvation layer of the ammonium group of Lys184 which is a residue conserved among the zinc β-lactamases and is thought to be important for substrate

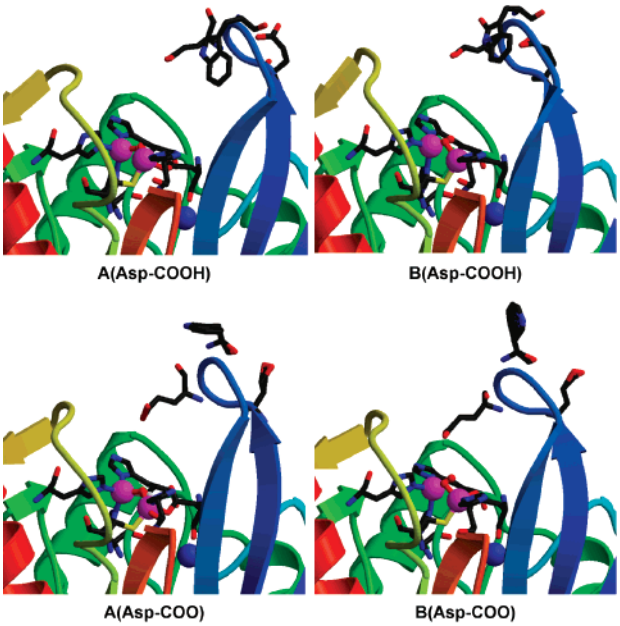

FIGURE 6: Average structure of the *B. fragilis* β-lactamase from the **A(Asp-COOH)**, **B(Asp-COOH)**, **A(Asp-COO)**, and **B(Asp-COO)** simulations. The structure is shown as a ribbon model (the loop of residues 41−52 is in blue). Trp49, Glu47, Glu45, and the zinc-coordinating residues are also shown. The zinc ions are displayed as magenta spheres, while the internal Na^+ ion is shown as a blue sphere with arbitrary radii.

binding. Some of these water molecules establish an organized network of hydrogen bonds during the simulations which interconnects the Nζ@Lys184 atom with the closest water molecule to Zn2, except for the **A(Asp-COO)** model. The most abundant Zn2−OH_2···$(H_2O)_n$···H−Nζ@Lys184 water bridges were linear sequences of H-bonds mediated by two (∼50% of the snapshots) or three water molecules (∼30%).

Conformation of the Active Site β-Hairpin Loop. According to NOE measurements in solution (*17*, *18*), the β-hairpin loop does not differ greatly in its relaxation behavior from the remainder of the protein. However, the position of the β-loop is changed and the motion of the Trp49 side chain is substantially reduced upon binding of a tight inhibitor (*17*).

The average structures of the active site region are shown for the various configurations in Figure 6. In all the configurations, the calculated rms flexibility of the active site β-hairpin loop is quite similar to that of other loops in the protein (see also Table 3). Intriguingly, for the **A(Asp-COOH)** model, the indole ring of Trp49 and the carboxylate group of Glu47 establish a Nε1@Trp49···Oε@Glu47 interaction with an average distance of 2.95 ± 0.25 Å. To make this contact, the Trp49 side chain moved from its initial position fully solvated into the vicinity of the zinc ions. The hydrogen bonding interaction with Glu47 resulted in a reduced mobility for the Trp49 side chain all along the **A(Asp-COOH)** trajectory in contrast with the NMR experiments which show that this residue is highly flexible. However, the AMBER and B3LYP/6-31+G* interaction energies for an indole−acetate dimer are −17.6 and −17.8 kcal/mol, respectively, and therefore, the presence of the Nε1@Trp49···Oε@Glu47 interaction is likely not a force field artifact. Furthermore, all along the **B(Asp-COOH)** trajectory, which was originally started from an equilibrated snapshot of **A(Asp-COOH)**, the Nε1@Trp49···Oε@Glu47 contact remained stable despite the larger flexibility of the β-hairpin loop in the **B(Asp-COOH)** configuration. Nevertheless, it might be that changes in the β-loop conformation involving the rupture of Trp49−Glu47 interaction would be beyond the time scale covered by our simulations (∼1 ns).

For the **A(Asp-COO)** model, the average structure of the loop is an extended conformation in which the Trp49 side chain, which is fully solvated by the surrounding water molecules, is highly flexible. For the **B(Asp-COO)** simulation, the β-loop partially acts as a "lid" to the zinc binding sites because of the Zn2−OH_2···OOC−Glu47 interaction observed in the **B(Asp-COO)** model (see Figure 6).

Overall, we conclude that the exact position of the active β-hairpin loop is sensitive to the global charge and the flexibility of the dinuclear active site. This dependence could well arise from the two negatively charged and flexible residues in the β-hairpin loop, Glu45 and Glu47.

Energetic Analysis. The structure of the dizinc clusters in selected snapshots along the MD trajectories was relaxed via QM/MM energy (PM3/AMBER) minimizations. The average values of some QM/MM distances involving the zinc centers are collected in Table 5. In general, the QM/MM dizinc clusters were structurally similar to those generated along the MD simulations using the MM force field representation. The average QM/MM Zn1−Zn2 distances are 3.65 and 3.51 Å for Zn1−OH−Zn2 models **A(Asp-COOH)** and **A(Asp-COO)**, respectively. These values are ∼0.2 Å larger than the MD−MM ones; that is, inclusion of polarization effects in the description of the zinc sites results in dizinc complexes that are more labile with respect to the Zn1−Zn2 separation. This is also observed in the **B(Asp-COOH)** and **B(Asp-COO)** models whose average Zn1−Zn2 distances at the QM/MM level are 4.86 and 4.55 Å, respectively (4.44 and 4.02 Å in the MM−MD averaged structures). We also observed that, in the **B(Asp-COO)** model, ∼50% of the QM/MM minimized structures disrupt the Zn1−OH···OOC−Asp103−Zn2 H-bond to give a bidentate adduct between Zn2 and the Asp103 carboxylate.

To assess the relative stability of the different models of the active site, we performed single-point PM3 D&C−PB calculations on subsystems comprising approximately one-third of the protein. These subsystems were built from the QM/MM relaxed structures along the MD trajectories. Table 5 shows the average heats of formation and solvation energies as estimated semiempirically. These values, which take into account the effects of the solvent continuum and the influence of structural fluctuations, can be combined to obtain a first estimation of the relative free energy differences (see Computational Methods). We note that systematic errors in the computed heats of formation and solvation free energies of one Zn1−OH−Zn2 bridged configuration are likely to partially cancel those of the corresponding nonbridged one.

The average free energy difference between the **A(Asp-COOH)** and **B(Asp-COOH)** configurations has a small value of ∼4 kcal/mol favoring the nonbridged state **B(Asp-COOH)**. Since the corresponding PM3 energy difference for cluster models in the gas phase is 8.3 kcal/mol favoring the rupture of the Zn1−OH−Zn2 bridge (6.0 kcal/mol at the B3LYP/6-31G* level), it turns out that the protein and solvent environment stabilizes the Zn1−OH−Zn2 bridged configuration by ∼4 kcal/mol. Nevertheless, the energy

Table 5: Average Values of Selected Interatomic Distances in Angstroms as Obtained from QM/MM Optimizations of the Dizinc Cluster in the Active Site[a]

model	H^0	ΔG^0_{solv}	G^0	Zn1−Zn2	Zn1−O1	Zn2−O1	Zn2−O3	Zn2−S	Zn2−N	Zn2−OW	O1−OW	O2−O1	Zn2−Na^+
A(Asp-COOH)	−3746	−727	−4472 ± 34	3.65	1.94	1.96	1.96	2.32	2.02	2.23	2.89	2.75	6.05
B(Asp-COOH)	−3770	−705	−4476 ± 31	4.86	1.90	3.56	1.92	2.18	1.96	1.92	2.67	2.67	5.59
A(Asp-COO)	−3855	−738	−4592 ± 33	3.51	1.91	1.92	1.91	2.25	1.99	3.98	2.99	2.81	5.42
B(Asp-COO)	−3830	−724	−4554 ± 35	4.55	1.88	3.50	1.90	2.26	1.98	1.93	2.92	2.98	5.66

[a] Average heats of formation and solvation energies in kilocalories per mole as obtained from linear scaling QM calculations are also indicated. Atom numbering as in Table 1.

difference between both configurations in the enzyme is clearly much smaller than the fluctuations of the individual energies (±35 kcal/mol). Therefore, we expect that a rapid interconversion process, **A(Asp-COOH) ↔ B(Asp-COOH)**, could well occur in the solvated protein. This energetic similarity of both configurations is also in agreement with their structural closeness as observed in the MD simulations. However, we note that **B(Asp-COOH)** could be further stabilized by entropy arising from its larger global flexibility (see Table 3).

With regard to the relative stability of the **A(Asp-COO)** and **B(Asp-COO)** configurations, we found that the presence of the Zn1−OH−Zn2 bridge makes the dizinc cluster in the **A(Asp-COO)** model ∼38 kcal/mol more stable than that in the **B(Asp-COO)** state. This energy difference in absolute value is larger than fluctuations in energy (±35 kcal/mol). The corresponding energy differences for the cluster models in the gas phase were 7.1 and 4.4 kcal/mol at the PM3 and B3LYP/6-31G* levels, respectively. Thus, the protein and solvent environment disfavors the rupture of the Zn1−OH−Zn2 bridge in the unprotonated Asp103 models. Furthermore, it may be reasonably expected that the **B(Asp-COO)** state would be inaccessible during the dynamic evolution of the more stable **A(Asp-COO)** state whose active site is predicted to be less susceptible to interconversion like in the **A(Asp-COOH) ↔ B(Asp-COOH)** models.

Structure and Dynamics of B. fragilis in the Absence of the Internal Na^+ Cation. To further examine the role of the internal cation, we carried out the **A(Asp-COOH)-noNa$^+$** simulation in which the Na^+ ion was replaced with an internal water molecule while the rest of the active site residues were in the **A(Asp-COOH)** configuration. The most important results obtained from this simulation regarding the structure of the dizinc complex, the solvation of the zinc ions, and the average position of the active site region are summarized in Figure 7. Other data (rmsd and rmsf values, etc.) are collected in Tables 2−4.

The absence of the buried Na^+ cation in the **A(Asp-COOH)-noNa$^+$** simulation slightly affects the internal geometry of the dizinc complex with respect to that in the **A(Asp-COOH)** state. For example, the mean Zn1−Zn2 distance (3.44 ± 0.10 Å) was only ∼0.04 Å shorter than in the presence of the internal Na^+. The zinc−ligand distances are very similar since the dizinc complexes in both states were described by the same force field. Throughout the **A(Asp-COOH)-noNa$^+$** simulation, the main chain of Asp69 has a strained conformation with a φ angle average of ∼56.3 ± 8°. Although this φ angle is still outside of the allowed range, it is ∼6° less positive than those observed for the rest of simulations in the presence of Na^+; that is, Asp69 adopts a less strained main chain conformation. Thus, the strained conformation of Asp69 is most likely linked to the presence of a salt bridge with the internal sodium ion. We also note that the **A(Asp-COOH)-noNa$^+$** trajectory may not be long enough to simulate the backbone motions required to fully relax the conformation of Asp69.

Most interestingly, the removal of the buried Na^+ influences the solvent structure and the flexibility of the active site β-hairpin loop. Throughout the **A(Asp-COOH)-noNa$^+$** simulation, we found that the Zn2 position lacks a well-defined first hydration shell of TIP3P water molecules as was observed for the **A(Asp-COOH)** state. The corresponding pair distribution function $g(r)$ shows a maximum at a Zn2−OW distance of 2.3 Å with an integrated value of only 0.30. This computational observation indicates that the hydration of the Zn2 ion in the Zn1−OH−Zn2 bridge could be facilitated by the presence of the buried positive charge adjacent to Zn2. On the other hand, the electrostatic change caused by removal of the internal sodium also affected the dynamics of the active site β-loop despite the large separation between the Na^+ position and the tip of the β-hairpin loop [note that the **A(Asp-COOH)** and **A(Asp-COOH)-noNa$^+$** simulations were started from the same initial structure]. In this case, the average position of the β-loop and the computed rmsf values of both the β-loop and the Trp49 residue were 1.11 and 0.67 Å, respectively, indicating that this part of the protein is clearly flexible and that the indole group of Trp49 was highly mobile and remained fully solvated during the dynamics.

DISCUSSION

Comparison with the Structure and Dynamics of B. fragilis Observed Experimentally. The comparative analysis of the most important zinc−ligand and residue−residue contacts observed in our MD simulations with those determined crystallographically can help us to further assess the ability of the different models to represent the active site of the *B. fragilis* enzyme. The **A(Asp-COOH)** model gives ion−residue and residue−residue contacts around Zn1, Zn2, and the internal Na^+ ion that are in excellent agreement with those observed in the 1ZNB crystal structure at pH 7.0 (see Figure 3). This model also has a Zn2-bound water molecule in contrast with the **A(Asp-COO)** model. Thus, the **A(Asp-COOH)** configuration with the neutral Asp103 most likely represents the active site of the *B. fragilis* enzyme as observed in the 1ZNB structure (*13*). However, this should not be construed as a global assignment because, for example, there are some uncertainties about the precise water coordination in the structure of *B. fragilis* obtained at pH 9.0 (*14*) which does not show a bridging ligand between the zinc ions.

To select the best model for representing the *B. fragilis* enzyme in solution, we can compare our theoretical predic-

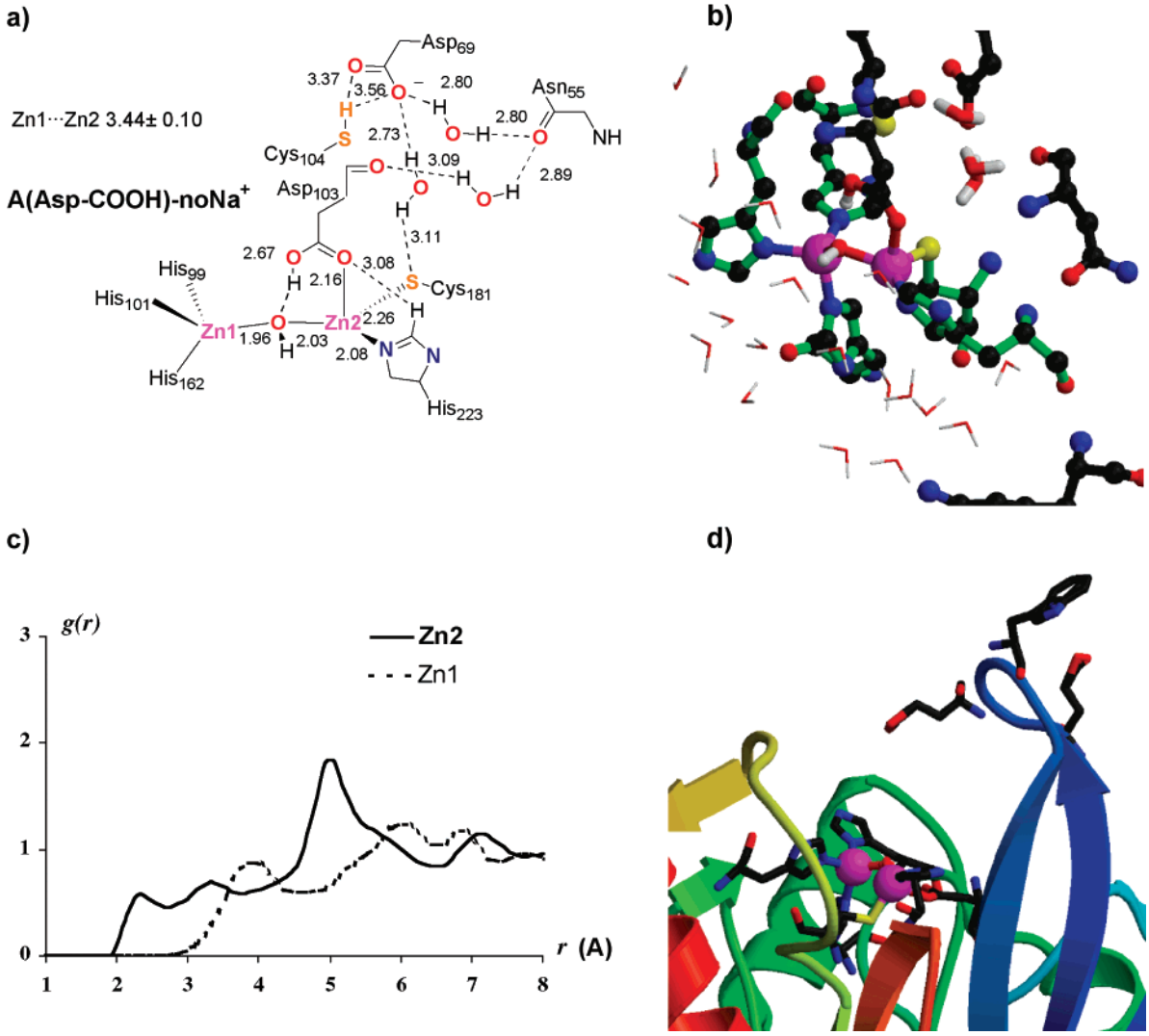

FIGURE 7: (a) Schematic representation of the most important interactions characterizing the active site of the **A(Asp-COOH)-noNa**$^+$ model. Some average distances between heavy atoms are given in angstroms. (b) Snapshot of the active site. (c) Plot of $g(r)$ for the zinc ions to the oxygens in the surrounding water molecules. (d) Average structure of the β-lactamase.

tions regarding protein flexibility with the NMR−NOE experimental data (*17*, *18*). In this respect, the conformation and mobility of the active site β-hairpin loop of residues 45−55 and the Trp49 indole group are of particular interest. Among the **A(Asp-COOH)**, **B(Asp-COOH)**, **A(Asp-COO)**, and **B(Asp-COOH)** models, the **A(Asp-COO)** configuration is the best one for representing the solvated *B. fragilis* enzyme given that, in this configuration, the Trp49 side chain is highly mobile in solution and the β-hairpin loop is fully extended. However, when the internal sodium is not present, the corresponding model [**A(Asp-COOH)-noNa**$^+$] also results in a flexible β-loop and a highly mobile Trp49 indole group (we note the NOE−NMR measurements were obtained in the absence of Na^+ in the NMR buffer). Therefore, a clear and definitive assignment of either **A(Asp-COO)** or **A(Asp-COOH)-noNa**$^+$ as the most likely state for the solvated protein cannot be made. Moreover, the fact that no single protein model reproduces all the structural features from X-ray and NMR−NOE experiments suggests that the exact configuration of the active site and the dynamics of the adjacent β-hairpin loop could be very dependent on environmental effects. This illustrates the complexity of the *B. fragilis* system.

Role of the Internal Na$^+$ *Ion.* Although kinetic measurements and/or enzyme purification procedures (*20*, *22*, *59*) were carried out in buffer solutions that included NaCl, the role an internal cation (i.e., Na^+ or Ca^{2+}) plays for the activity of the *B. fragilis* zinc β-lactamase in vivo remains unclear. Nevertheless, our simulations have provided insights into the possible role of the internal Na^+ ion. The remarkable dynamical stability of the Na^+ coordination polyhedron along the different trajectories suggests that the *B. fragilis* protein is well adapted to bind the internal Na^+ ion and that this ion plays an important structural role. We also found that the buried salt bridge between the Na^+ ion and the conserved Asp69 residue is involved in the strained conformation of the Asp69 main chain. All of these results suggest that an internal positive charge close to Zn2 should exist in the wild-type enzyme under physiological conditions. This hypothesis is in agreement with recent kinetic experiments on the Cys104Arg mutant of the *B. fragilis* dizinc enzyme (*22*). Specifically, by introduction of this mutation, it has been shown that the two zinc ions are still bound by the enzyme. This retention of the zinc binding ability can be understood if the positively charged side chain of Arg displaces an internally bound cation which would then leave

the global charge of the protein unchanged by the Cys104Arg mutation.

Flexibility of the Zn1−OH−Zn2 Bridge. The QM calculations summarized in Figures 1 and 2 and those reported in previous work (*27*, *28*) demonstrate that the dizinc cluster models can readily interchange between a Zn1−OH−Zn2 bridged state and a nonbridged state in which the Zn1 and Zn2 environments interact through H-bond contacts. Clearly, these results suggest that the zinc ion cluster in the *B. fragilis* active site could be present in distinct states, which likely would affect substrate binding and catalysis. To further assess this point, it was important to take into account the energetic and geometrical influence of the protein environment and solvent. Our MD simulations of the different protein configurations and the energetic analyses carried out at the PM3 semiempirical level have given us an estimate of the role the environment plays. In particular, the calculations have allowed us to understand the geometrical and energetic consequences of the **A(Asp-COOH) ↔ B(Asp-COOH)** and **A(Asp-COO) ↔ B(Asp-COO)** rearrangements.

The active site in the **A(Asp-COOH)** and **B(Asp-COOH)** simulations had stable contacts that were favorable for promoting the breaking and formation, respectively, of the Zn1−OH−Zn2 bridge. For example, the Zn2 site remains solvent accessible during the **A(Asp-COOH)** simulation which allows bulk water molecules to enter the active site region and destabilize the Zn1−OH−Zn2 bridge. The coordination spheres of the Zn1 and Zn2 ions along the **B(Asp-COOH)** simulation were bound through long-lived H-bond interactions in which the Zn1−hydroxide moeity interacted with Asp103 and Zn2−OH_2 moiety. In other words, the Zn−OH moiety was favorably positioned to ligand exchange at the Zn2 site, thereby regenerating the Zn1−OH−Zn2 bridge. Other structural features of the **A(Asp-COOH)** and **B(Asp-COOH)** simulations (e.g., the similar dynamics of the active site β-hairpin loop) appear compatible with a fast interconversion between the two states. These geometrical and dynamical insights are in agreement with the data obtained from the energetic analyses. The average free energy ($G° \approx H° + \Delta G^0_{solv}$) of both configurations was very similar as estimated by PM3 semiempirical calculations. In this case, the **A(Asp-COOH) ↔ B(Asp-COOH)** interconversion is isoenergetic, although the **B(Asp-COOH)** state might be entropically favored.

For the **A(Asp-COO)** and **B(Asp-COO)** configurations, the geometrical and energetic analyses predict that **A(Asp-COO)** has a strong Zn1−OH−Zn2 bridge and that relatively large geometrical changes are involved in the **A(Asp-COO) → B(Asp-COO)** rearrangement. Most importantly, the **B(Asp-COO)** state is predicted to be ∼38 kcal/mol less stable than the **A(Asp-COO)** state according to the average PM3 energies. The reason for this is the apparent inability of the *B. fragilis* active site to stabilize a heterogeneous system in which one zinc ion and its ligands bear a +1 charge while the other zinc ion and its ligands are neutral as is the case for the **B(Asp-COO)** state. This difference does not arise in the **B(Asp-COOH)** model because both zinc sites bear a global charge of +1.

Our energetic analyses can discriminate among the different models in terms of the flexibility of the Zn1−OH−Zn2 interaction. The model with the unprotonated Asp103 results in a rigid Zn1−OH−Zn2 linkage (Zn1−Zn2 distance < 3.5 Å), whereas the neutral Asp103 is compatible with a fluctuating Zn1−Zn2 distance (3.5 < Zn1−Zn2 distance < 4.5 Å). Interestingly, the low-temperature EPR spectrum for the Co(II)-substituted *B. fragilis* enzyme indicates that the two metal binding sites do not interact with each other to form a magnetically coupled dinuclear active site (*60*). The EPR signal disappears at temperatures higher than 50 K which also suggests that the metal binding sites are flexible in consonance with the proposed **A(Asp-COOH) ↔ B(Asp-COOH)** equilibrium. However, more experimental and theoretical work on the flexibility of the Zn1−OH−Zn2 bridge in the solvated protein will be required to definitively determine the dynamical properties of the zinc ions in the unbound form of the metallo-β-lactamases.

***A(Asp-COOH) ↔ B(Asp-COOH)** as the Kinetically Active Configurations of the Active Site.* The hypothetical equilibrium between the **A(Asp-COOH)** and **B(Asp-COOH)** configurations should be more favorable for substrate binding and catalysis than the rigidity exhibited by the **A(Asp-COO)** state. In the **A(Asp-COOH)** and **B(Asp-COOH)** simulations, the flexibility of the dizinc cluster only slightly affects the positioning and dynamics of other residues involved in substrate binding (*13*, *14*) (e.g., the ammonium group of Lys185, the hydrophobic pocket formed by Val52, Ile46, and Ile72, the conformation of the β-hairpin loop, etc.). Furthermore, the rupture of the Zn1−OH−Zn2 bridge in the presence of the substrate is a requirement for the Zn1-bound nucleophile to attack the β-lactam carbonyl group (*59*). Although the **A(Asp-COOH) ↔ B(Asp-COOH)** equilibrium could be influenced by protein−substrate contacts (e.g., by ligation of the β-lactam N atom to Zn2), our results reveal that it is also possible for the unbound form of the *B. fragilis* enzyme to evolve through configurations suitable for nucleophilic attack. Alternatively, once the substrate is bound, the **A(Asp-COO) ↔ B(Asp-COO)** equilibrium could be shifted to the right, but we estimate that this binding process would have to overcome a very significant energetic penalty (∼38 kcal/mol).

The hypothesis that Asp103 is neutral in the native form of the *B. fragilis* enzyme helps interpret the mutagenesis experiments at position 103. As mentioned in the introductort section, mutation of Asp103 to *neutral* polar residues such as asparagine and serine leads to mutant enzymes that retain the ability to bind 2 equiv of Zn(II). The Asp103Asn and Asp103Ser mutants also catalyze the hydrolysis of penicillin G, having k_{cat} values that are $^1/_2$ of and 10^2-fold lower than wild-type values (∼$^1/_2$ of and 10^5-fold lower for imipenem as a substrate). If we assume that the **A(Asp-COOH)** and **B(Asp-COOH)** models represent the structure of wild-type *B. fragilis*, the mutation of the neutral Asp103 residue into Asn or Ser would not change the global charge of the active site which explains the metal binding ability and the catalytic activity of the mutant enzymes. In addition, the greater efficiency of the Asp103Asn mutant with respect to Asp103Ser is due to the ability of the asparagine side chain to establish a Zn1−OH···H_2N−C═O−Zn2 contact (i.e., similar to a Zn1−OH···HO−C═O−Zn2 contact) that assists in positioning the Zn2 site with respect to the Zn1-bound nucleophile.

SUMMARY AND CONCLUSIONS

The active site of the *B. fragilis* zinc-β-lactamase has been studied by means of QM calculations on cluster models and

a series of MD simulations assuming five different active site configurations. When the results from the MD simulations are compared with those from X-ray and NMR−NOE data, a single protein configuration cannot be assigned, suggesting thus that the protonation state and structure of the dizinc complex could be dependent on relatively small environmental changes. For the crystallographic structure at pH 7, the best model corresponds to the **A(Asp-COOH)** simulation which presents the Zn1−OH−Zn2 bridge with a protonated Asp103 residue. In aqueous solution, however, two MD trajectories corresponding to the **A(Asp-COO)** model (i.e., unprotonated Asp103) and the **A(Asp-COOH)-noNa$^+$** configurations (i.e., protonated Asp103 in the absence of the internal Na^+ ion) are compatible with the conformation and mobility of the active site β-hairpin loop as observed via NMR−NOE experiments. Nevertheless, the comparative structural analyses among the different MD trajectories augmented with the energetic calculations have provided novel insights into the structure of the *B. fragilis* active site. (1) Our simulations confirm that the *B. fragilis* protein can efficiently bind the internal Na^+ ion observed crystallographically. This clearly indicates that a buried cation should play an important structural role in vivo. (2) In the solvated protein, we predict that the unprotonated Asp103 results in a rigid Zn1−OH−Zn2 linkage whereas the neutral Asp103 is compatible with a fluctuating Zn1−Zn2 distance through the breaking and/or formation of the Zn1−OH−Zn2 bridge. (3) If it is assumed that a flexible Zn1−OH−Zn2 bridge would be more favorable for substrate binding and catalysis, we propose that the kinetically active form of the *B. fragilis* enzyme involves an equilibrium between the **A(Asp-COOH)** and **B(Asp-COOH)** configurations. (4) This proposal, which implies that Asp103 would be neutral in the native form of the *B. fragilis* enzyme, can also explain the ability of the Asp103Asn and Asp103Ser *B. fragilis* mutants to bind 2 equiv of Zn(II) and to retain some enzymatic activity.

SUPPORTING INFORMATION AVAILABLE

RESP atomic charges and force constants used to build the MM models of the zinc ions in the different models, plots showing the rms deviation between the instantaneous computed structures and the 1ZNB crystal structure as a function of time in the different simulations, and a figure showing the superposition of the average protein structures in the different models. This material is available free of charge via the Internet at http://pubs.acs.org.

REFERENCES

1. Walsh, C. (2000) *Nature 406*, 775−781.
2. Wright, G. D. (2000) *Chem. Biol. 7*, 127−132.
3. Waley, S. G. (1992) in *The Chemistry of β-Lactams* (Page, M. I., Ed.) pp 199−227, Blackie Academic&Professional, London.
4. Matagne, A., Lamotte-Brasseur, J., and Frère, J. M. (1998) *Biochem. J. 330*, 581−598.
5. Livermore, D. M., and Woodford, N. (2000) *Curr. Opin. Microbiol. 3*, 489−495.
6. Wang, Z., Fast, W., Valentine, A. M., and Benkovic, S. J. (1999) *Curr. Opin. Chem. Biol. 3*, 614−622.
7. Bush, K. (1998) *Clin. Infect. Dis.*, S48−S53.
8. Prosperi-Meys, C., Llabres, G., de Seny, D., Paul-Soto, R., Hernández-Valladares, M., Laraki, N., Frère, J. M., and Galleni, M. (1999) *FEBS Lett. 443*, 109−111.
9. Haruta, S., Yamaguchi, H., Yamamoto, E. T., Eriguchi, Y., Nukaga, M., O'Hara, K., and Sawai, T. (2000) *Antimicrob. Agents Chemother. 44*, 2304−2309.
10. Poirel, L., Naas, T., Nicolas, D., Collet, L., Bellais, S., Cavallo, J. D., and Nordmann, P. (2000) *Antimicrob. Agents Chemother. 44*, 891−897.
11. Tsakris, A., Pournaras, S., Woodford, N., Palepou, A. F. I., Babini, G. S., Douboyas, J., and Livermore, D. M. (2000) *J. Clin. Microbiol. 38*, 1290−1292.
12. Lauretti, L., Riccio, M. L., Mazzariol, A., Cornaglia, G., Amicosante, G., Fontana, R., and Rossolini, G. M. (1999) *Antimicrob. Agents Chemother. 43*, 1584−1590.
13. Concha, N. O., Rasmussen, B. A., Bush, K., and Herzberg, O. (1996) *Structure 4*, 623−635.
14. Carfi, A., Duée, E., Paul-Soto, R., Galleni, M., Frère, J. M., and Dideberg, O. (1998) *Acta Crystallogr. D54*, 47−57.
15. Fitzgerald, P. M. D., Wu, J. K., and Toney, J. H. (1998) *Biochemistry 37*, 6791−6800.
16. Toney, J. H., Fitzgerald, P. M. D., Grover-Sharma, N., Olson, S. H., May, W. J., Sundelof, J. G., Vanderwall, D. E., Cleary, K. A., Grant, S. K., Wu, J. K., Kozarich, J. W., Pompliano, D. L., and Hammond, G. G. (1998) *Chem. Biol. 5*, 185−196.
17. Scrofani, S. D. B., Chung, J., Huntley, J. J. A., Benkovic, S. J., Wright, P. E., and Dyson, H. J. (1999) *Biochemistry 38*, 14507−14514.
18. Huntley, J. J. A., Scrofani, S. D. B., Osborne, M. J., Wright, P. E., and Dyson, H. J. (2000) *Biochemistry 39*, 13356−13364.
19. Li, Z., Rasmussen, B. A., and Herzberg, O. (1999) *Protein Sci. 8*, 249−252.
20. Yanchak, M. P., Taylor, R. A., and Crowder, M. W. (2000) *Biochemistry 39*, 11330−11339.
21. Yang, Y., Keeney, D., Tang, X., Canfield, N., and Rasmussen, B. A. (2000) *J. Biol. Chem. 274*, 15706−15711.
22. Fast, W., Wang, Z., and Benkovic, S. J. (2001) *Biochemistry 40*, 1640−1650.
23. Crowder, M. W., Wang, Z., Franklin, S. L., Zovinka, E. P., and Benkovic, S. J. (1996) *Biochemistry 35*, 12126−12132.
24. Paul-Soto, R., Bauer, R., Frère, J. M., Galleni, M., Meyer-Klauche, W., Nolting, H., Rossolini, G. M., de Seny, D., Hernández-Valladares, M., Zeppezauer, M., and Adolph, H. W. (1999) *J. Biol. Chem. 274*, 13242−13249.
25. Paul-Soto, R., Hernández-Valladares, M., Galleni, M., Bauer, R., Zeppezauer, M., Frère, J. M., and Adolph, H. W. (1998) *FEBS Lett. 438*, 137−140.
26. Salsbury, F. R., Crowley, M. F., and Brooks, C. L. (2001) *Proteins: Struct., Funct., Genet. 44*, 448−459.
27. Díaz, N., Suárez, D., and Merz, K. M., Jr. (2000) *J. Am. Chem. Soc 122*, 4197−4208.
28. Krauss, M., Gilson, H. R. S., and Gresh, N. (2001) *J. Phys. Chem. B 105*, 8040−8049.
29. Yang, W., and Lee, T.-S. (1995) *J. Chem. Phys. 103*, 5674−5678.
30. Dixon, S. L., and Merz, K. M., Jr. (1997) *J. Chem. Phys. 107*, 879−893.
31. Hehre, W. J., Radom, L., Schleyer, P. v. R., and Pople, J. A. (1986) *Ab Initio Molecular Orbital Theory*, John Wiley & Sons, New York.
32. Becke, A. D. (1995) in *Modern Electronic Structure Theory Part II* (Yarkony, D. R., Ed.) World Scientific, Singapore.
33. Rasolov, V. A., Pople, J. A., Patner, M. A., and Windus, T. L. (1998) *J. Chem. Phys. 109*, 1223−1230.
34. Frisch, M. J., Trucks, G. W., Schlegel, H. B., Scuseria, G. E., Robb, M. A., Cheeseman, J. R., Zakrzewski, V. G., Montgomery, J. A., Stratmann, J. R. E., Burant, J. C., Dapprich, S., Millam, J. M., Daniels, A. D., Kudin, K. N., Strain, M. C., Farkas, O., Tomasi, J., Barone, V., Cossi, M., Cammi, R., Mennucci, B., Pomelli, C., Adamo, C., Clifford, S., Ochterski, J., Petersson, G. A., Ayala, P. Y., Cui, Q., Morokuma, K., Malick, D. K., Rabuck, A. D., Raghavachari, K., Foresman, J. B., Cioslowski, J., Ortiz, J. V., Stefanov, B. B., Liu, G., Liashenko, A., Piskorz, P., Komaromi, I., Gomperts, R., Martin, R. L., Fox, D. J., Keith, T., Al-Laham, M. A., Peng, C. Y., Nanayakkara, A., Gonzalez, C., Challacombe, M., Gill, P. M. W., Johnson, B., Chen, W., Wong, M. W., Andres, J.

L., Gonzalez, C., Head-Gordon, M., Replogle, E. S., and Pople, J. A. (1998) *Gaussian 98*, Gaussian, Pittsburgh, PA.
35. Reed, A. E., Weinstock, R. B., and Weinhold, F. (1985) *J. Chem. Phys. 83*, 735−746.
36. Stewart, J. J. P. (1989) *J. Comput. Chem. 10*, 209−220.
37. Stewart, J. J. P. (1991) *J. Comput. Chem. 12*, 320−341.
38. Brothers, E. N., Suárez, D., Deerfield, D. W., and Merz, K. M. (2002) *J. Comput. Chem.* (in press).
39. Dixon, S. L., van der Vaart, A., Gogonea, V., Vincent, J. J., Brothers, E. N., Suárez, D., Westerhoff, L. M., and Merz, K. M. J. (1999) *DivCon 99*, The Pennsylvania State University, University Park, PA.
40. Suárez, D., and Merz, K. M., Jr. (2001) *J. Am. Chem. Soc. 123*, 3759−3770.
41. Hoops, S. C., Anderson, K. W., and Merz, K. M., Jr. (1991) *J. Am. Chem. Soc. 113*, 8262−8270.
42. Ryde, U. (1995) *Proteins 21*, 40−56.
43. Schafmeister, C., Ross, W. S., and Romanovski, V. (1995) *LEaP*, University of California, San Francisco.
44. Cornell, W. D., Cieplak, P., Bayly, C. I., Gould, I. R., Merz, K. M., Jr., Ferguson, D. M., Spellmeyer, D. C., Fox, T., Caldwell, J. W., and Kollman, P. A. (1995) *J. Am. Chem. Soc. 117*, 5179−5197.
45. Case, D. A., Pearlman, D. A., Caldwell, J. W., Cheatham, T. E., II, Ross, W. S., Simmerling, C. L., Darden, T. A., Merz, K. M., Jr., Stanton, R. V., Cheng, A. L., Vincent, J. J., Crowley, M., Ferguson, D. M., Radmer, R. J., Seibel, G. L., Singh, U. C., K., W. P., and Kollman, P. A. (1997) *AMBER*, version 6.0, University of California, San Francisco.
46. van Gunsteren, W. F., and Berendsen, H. J. C. (1977) *Mol. Phys. 34*, 1311.
47. Allen, M. P., and Tildesley, D. J. (1987) *Computer Simulation of Liquids*, Clarendon Press, Oxford, U.K.
48. Berendsen, H. J. C., Potsma, J. P. M., van Gunsteren, W. F., DiNola, A. D., and Haak, J. R. (1984) *J. Chem. Phys. 81*, 3684−3690.
49. Essman, V., Perera, L., Berkowitz, M. L., Darden, T., Lee, H., and Pedersen, L. G. (1995) *J. Chem. Phys. 103*, 8577−8593.
50. Petersen, H. G. (1995) *J. Chem. Phys. 103*, 3668−3679.
51. Kraulis, P. J. (1991) *J. Appl. Crystallogr. 24*, 946−950.
52. Merritt, E. A., and Bacon, D. J. (1997) *Methods Enzymol. 277*, 505−524.
53. Cheng, A., Stanton, R. S., Vincent, J. J., van der Vaart, A., Damodaran, K. V., Dixon, S. L., Hartsough, D. S., Mori, M., Best, S. A., Monard, G., Garcia, M., Van Zant, L. C., and Merz, K. M. J. (1999) *ROAR*, version 2.0, The Pennsylvania State University, University Park, PA.
54. Gogonea, V., and Merz, K. M., Jr. (1999) *J. Phys. Chem. A 103*, 5171−5178.
55. van der Vaart, A., Suárez, D., and Merz, K. M., Jr. (2000) *J. Chem. Phys. 113*, 10512−10523.
56. Zhan, C. G., de Souza, N., Rittenhouse, R., and Ornstein, R. (1999) *J. Am. Chem. Soc. 121*, 7279−7282.
57. Ullah, J. H., Walsh, T. R., Taylor, I. A., Emery, D. C., Verma, C. S., Gamblin, S. J., and Spencer, J. (1998) *J. Mol. Biol. 284*, 125−136.
58. Díaz, N., Suárez, D., and Merz, K. M., Jr. (2000) *Chem. Phys. Lett. 326*, 288−292.
59. Wang, Z., Fast, W., and Benkovic, S. J. (1999) *Biochemistry 38*, 10013−10023.
60. Wang, Z., and Benkovic, S. J. (1998) *J. Biol. Chem. 273*, 22402−22408.

BI0121860